Earth and Planetary Science Letters 520 (2019) 50–62

Contents lists available at ScienceDirect

Earth and Planetary Science Letters

www.elsevier.com/locate/epsl

The nature of the subduction wedge in an erosive margin: Insights from the analysis of aftershocks of the 2015 Mw 8.3 Illapel earthquake beneath the Chilean Coastal Range

Diana Comte [a,*], Marcelo Farias [b], Steven Roecker [c], Raymond Russo [d]

[a] Departamento de Geofísica, Advanced Mining Technology Center, Facultad de Ciencias Físicas y Matemáticas, Universidad de Chile, Blanco Encalada 2002, Santiago, Chile
[b] Departamento de Geología, Facultad de Ciencias Físicas y Matemáticas, Universidad de Chile, Plaza Ercilla 803, Santiago, Chile
[c] Rensselaer Polytechnic Institute, Troy, NY 12180, USA
[d] Department of Geological Sciences, University of Florida, Gainesville, FL 32611, USA

ARTICLE INFO

Article history:
Received 9 February 2019
Received in revised form 17 May 2019
Accepted 21 May 2019
Available online xxxx
Editor: R. Bendick

Keywords:
active continental margin
fore-arc subduction erosion
Andean arc
seismic tomography
Illapel earthquake
aftershocks

ABSTRACT

Aftershocks of the 16 September 2015 M8.3 Illapel earthquake in central Chile were recorded for a period of one year by the Chile-Illapel Aftershock Experiment (CHILLAX) seismic network. An initial catalog of about 100,000 events was generated by a novel automated picking algorithm that combines an auto-regressive detection/onset estimation method with some recently developed windowing techniques. We combine arrival times of P and S waves from about 9,000 of the best recorded of these events with relative arrival times of teleseismic P waves and phase delays of Rayleigh waves recovered from ambient noise to generate a three-dimensional image of P and S wavespeeds in that part of the Andean margin located beneath the network. Hypocenters of aftershocks located in the final model appear to be grouped into four distinct zones: two lower parallel zones that dip about 20° to the east, an upper, highly active zone that dips about 30° to the east, and a diffuse zone of smaller events located between this upper zone and the surface. Nearly all of the events with M > 4 are located at the bottom edge of the highly active zone and define a plane dipping about 26° to the east. Most of these events have almost identical thrust mechanisms and are separated from the lower zones by a steep gradient in increasing wavespeeds. The lower end of the upper zone, at about 55 km depth, is marked by another velocity gradient dipping to the west that bounds the diffuse shallow activity and projects to the surface west of the high Andes. We postulate that the triangular region delimited by these two high wavespeed gradients is a subduction wedge, generated by the removal of material from the leading edge of the upper plate by subduction erosion, and subsequently underplated back on to the overriding plate at depth. This model explains many of the features we observe in the seismicity and wavespeeds and is consistent with geologic observations of uplift and extension in this part of the Chilean coastal margin. Characteristics of this wedge, such as its shape and the lack of correlation with the coeval back-arc tectonic setting, suggest that high Andes are not directly coupled with the behavior of the subduction interface.

1. Introduction

Aftershocks of large earthquakes generally are presumed to be caused by asperities or other sources of residual strain on the mainshock rupture surface, and analyses of these events typically focus on how strain is released on that surface. Moreover, the rate of aftershock activity is usually significantly higher than that of the ambient background, which allows an extensive dataset to be recorded by a short-term seismic network. Hence, in addition to investigating the mainshock, aftershock surveys provide rare opportunities to illuminate the tectonics of the region in which the mainshock occurred.

The 16 September 2015 M8.3 Illapel earthquake ruptured along the boundary between the Nazca and South American plates between about 30° and 32°S (Fig. 1). It extended about 140 km eastwards from the trench and from the near surface to about 50 km depth (Tilmann et al., 2016). The double couple component of

* Corresponding author.
E-mail address: dcomte@dgf.uchile.cl (D. Comte).

https://doi.org/10.1016/j.epsl.2019.05.033
0012-821X/

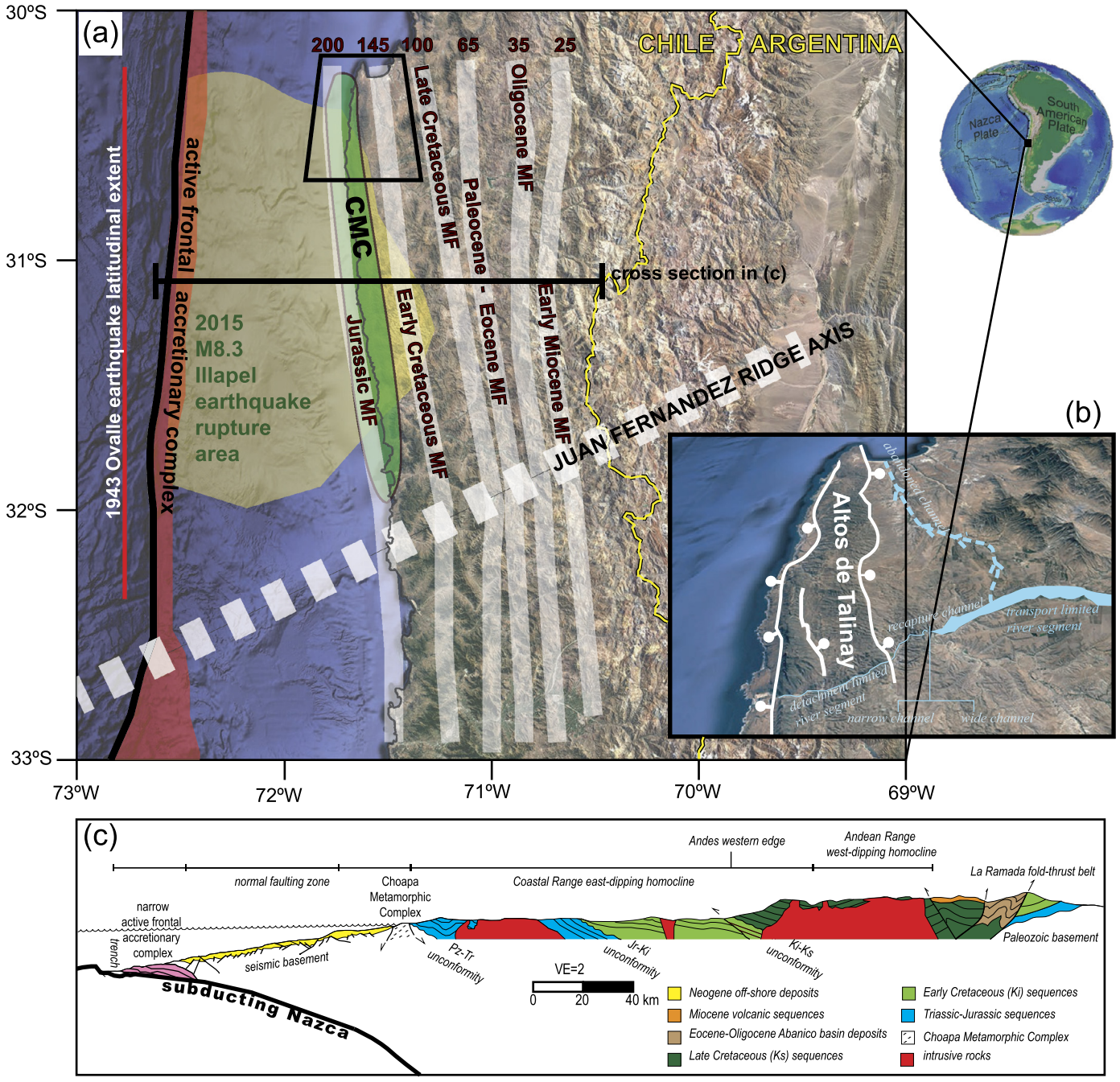

Fig. 1. (a) Map of the study region. Positions of magmatic fronts between the Jurassic and the early Miocene, determined by the westernmost extent of corresponding plutonic rocks outcrops (based on Parada et al., 1988), are shown as N-S oriented grey lines with their age in m.y. and period/epoch indicated. Yellow region delimits the main rupture area of the Illapel earthquake (Tilmann et al., 2016). The rupture length of the 1943 Ovalle earthquake is shown with a red line. (b) Oblique view to the north of the Altos de Talinay region bounded by the black trapezoid in (a) showing the main normal/vertical faults along which core basement rocks uplifted, as shown by marine terraces (e.g., Saillard et al., 2009). These terraces temporarily deflected the paleo-Limari river (dashed blue line) into Tongoy bay. The river has since reoccupied its original channel (solid blue line) to the sea. (c) Simplified geological cross-section along line A–A′ in (a) locating features referred to in the text. Offshore structure and geology are after Becerra et al. (2016), while onshore geology is modified from the compilation made by Rodriguez et al. (2018). (For interpretation of the colors in the figure(s), the reader is referred to the web version of this article.)

the CMT solution[1] indicates a low angle thrust dipping 19° to the ENE with a rake of 83°. The hypocentral depth is about 22 km, and most of the moment release occurred offshore between the coast and the trench. Nevertheless, that part of the rupture zone between about 20–50 km depth, along with the ambient seismicity of the subduction zone to depths of 120 km, extended beneath the entirety of Chile to its border with Argentina. Within a few days of the Illapel earthquake, seismologists from the Departamento de Geofísica (DGF) at the Universidad de Chile installed a network of 16 short period seismometers above the rupture zone beneath Chile (Fig. 2). In mid-November 2015, an international team (Chile/US) replaced this short period network with 20 broad band sensors (Guralp CMG-3T) that operated for a period of about one year. This combined network, referred to as the Chile-

[1] https://earthquake.usgs.gov/earthquakes/eventpage/us20003k7a#moment-tensor.

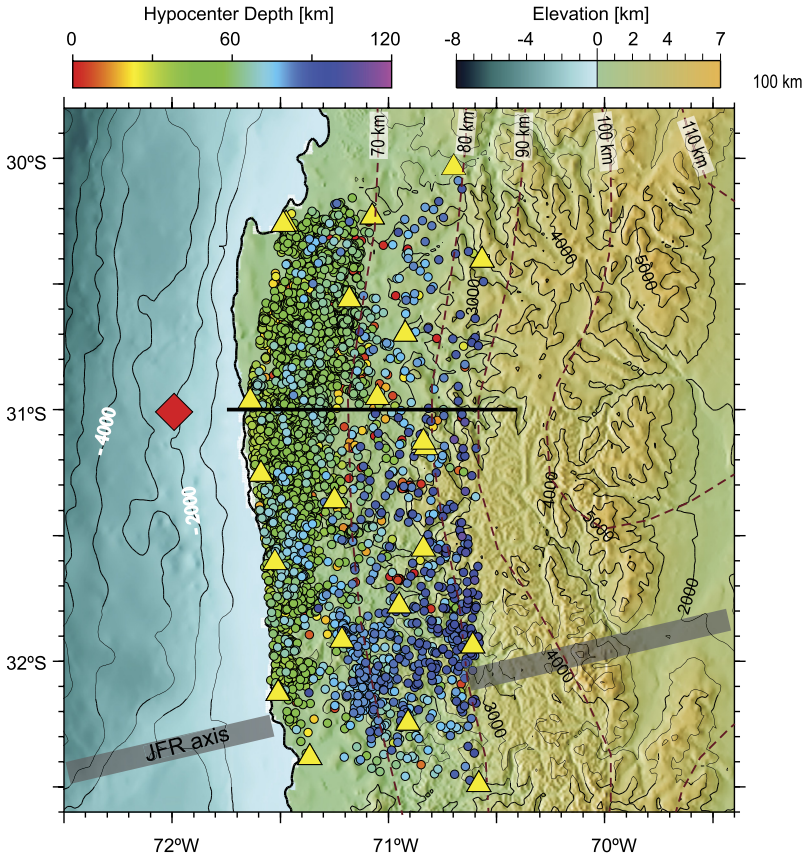

Fig. 2. Map of the Norte-Chico region with elevations shaded and contoured at 1000 m intervals. Stations of the CHILLAX network are indicated by yellow triangles. The location of the main rupture zone of the Illapel mainshock as determined by the USGS Earthquake Hazards Program (https://earthquake.usgs.gov/earthquakes/eventpage/us20003k7a/finite-fault) is shown by a large red diamond. The black bar at 31°S delimits the cross sections shown in Figs. 3, 4, S6, and S7. Locations of the 9,000 local earthquakes used in this study shown by filled circles with colors corresponding to depth as indicated in the palette at the top of the figure. A projection of the Juan Fernandez Ridge to the east of the trench is plotted as a gray bar. Dashed lines show isodepths of the top of the slab determined by Anderson et al. (2007).

Illapel Aftershock Experiment (CHILLAX), recorded an average of 300 events per day in the vicinity of the Illapel rupture zone.

The Illapel earthquake appears to be a repeat of the 1943 M8.3 Ovalle earthquake, although the 1943 event may have been significantly smaller in magnitude (Tilmann et al., 2016). The Illapel rupture and aftershocks are bounded to the south by the intersection of the Juan Fernandez Ridge (JFR) with the trench, which also marks the northern end of the rupture zone of the 2010 M8.8 Maule earthquake. Of particular interest to this study, this area is considered to be one of the better examples of a subduction erosive margin (e.g., von Huene and Scholl, 1991), due to the progressive landward migration of the magmatic front and the lack of deformed sediments associated with an accretionary prism (e.g., Rutland, 1971). For the most part, inferences about the structure controlling the subduction erosion processes have come from active seismic experiments that image the upper 20 km of the seismogenic zone near the trench. In contrast, megathrust earthquakes and their aftershocks rupture to depths of about 60 km, and so provide an opportunity to investigate the potential role of deeper structures in these processes through passive seismic investigations.

Here, we analyze data from the CHILLAX deployment in a joint inversion of local and teleseismic body wave arrival times with phase velocity dispersion curves of fundamental mode Rayleigh waves to generate three-dimensional images of P and S wavespeeds within the subduction wedge. We combine those images with hypocenter locations and focal mechanisms to illuminate the properties of subduction wedges in an erosive margin.

2. Geotectonic background

The Illapel earthquake occurred within the north central or "Norte Chico" part of the Chilean margin (~29–32°S; Fig. 1). During Devonian times, Norte Chico was part of the passive margin of western Gondwana. Sedimentary deposition along this margin took place over a long period of time (over 50 m.y.), and these deposits were accreted to the continental margin when subduction began in late Paleozoic times (Rebolledo and Charrier, 1994; Willner et al., 2008). The remnants of this accretionary complex now appear along the coast in sparse outcrops of the Choapa Metamorphic Complex (CMC).

Since Jurassic times, one of the main features of the geological evolution of this region has been the eastward migration of the magmatic arc (e.g., Rutland, 1971; Aguirre et al., 1974; Kay and Mpodozis, 2002) from near the current coastline to the current Pacific-Atlantic drainage divide (Fig. 1a). Between Jurassic and Early Cretaceous times, the margin was characterized by the development of back-arc extensional basins, partially inverted and shortened during Late Cretaceous and the Paleocene times (e.g., Mpodozis and Ramos, 1990; Charrier et al., 2015). The Eocene period marked a revival of extensional tectonics, inverted in the Early Miocene and propagated to the east, forming the La Ramada fold and thrust belt near the international boundary (see Charrier et al., 2015, and references therein). Subsequently, the Andean deformation front migrated rapidly eastward to its current position east of the Pampean Range, about 800 km from the trench, forming what has been termed a broken foreland basin.

The recent evolution of this area is characterized by uplift and vertical/normal faulting along the coast coeval with exhumation in the Andes (Rodríguez et al., 2018). Active seismic imaging of offshore geology also shows pervasive normal faulting, the sense of which is mainly antithetic to subduction near the trench, and with different polarities near the coast, with some structures showing gentle tectonic inversion (Becerra et al., 2016). Marine terraces provide evidence of rapid uplift of the coast during the Quaternary, which deflected the paleo-Limari river into Tongoy bay (Fig. 1). The Limari river has since been recaptured by its original outlet to the sea.

Currently, the oceanic Nazca plate subducts beneath the continental South American plate along the Norte Chico margin at a rate of 63 mm/yr in a N81°E direction (e.g., Kreemer et al., 2014). In the southern part of this region, the upper part of the subducting slab beneath Chile appears to dip at about 20° before becoming subhorizontal near 100 km depth beneath Argentina (e.g., Mulcahy et al., 2014). This Pampean "flat slab" region is aligned with the JFR, which, because aseismic ridges are generally less dense than normal oceanic lithosphere, is often cited as the cause of the flattening. The arrival of the JFR at the trench in the late Miocene coincides with the extinction of arc volcanism in this region. The JFR is also believed to be responsible for the eastward age-migration of adakitic volcanism (e.g., Kay and Mpodozis, 2002), the uplift of the Pampean Range with a deformational front nearly 800 km east of the trench, and the local absence of the Central Depression, the forearc basin that is well-developed north and south of this region (e.g., Jordan et al., 1983). Instead, the Norte Chico region is physiographically characterized by two orographic belts, the Coastal Cordillera and the Andes, divided by a decrease in elevation that has been interpreted as a proto-Central Depression (proto-forearc basin) (Farias et al., 2008).

The Norte Chico lacks a significant frontal accretionary complex, and the sedimentary column in the neighboring trench over the Nazca plate is either absent or very thin (e.g., Becerra et al., 2016) (Fig. 1). This lack of sediment has been ascribed to long-term aridity that limited erosion and transport of sediment into the trench since at least Miocene times (Carretier et al., 2013; Rodríguez et al., 2018). Alternatively, subducting seamounts on the oceanic slab may have caused frontal subduction erosion (e.g., von Huene et al., 2004). A third possibility is that the JFR has acted as a barrier to the northward transport of sediment in the trench (von Huene et al., 1997).

While flat slab subduction associated with the JFR is often invoked to explain various evolutionary features of the Andes, certain Andean developments preceded the arrival of the JFR in the late Miocene. In particular, the frontal magmatic arc migrated to the east with respect to the previously developed arc in Norte Chico since Jurassic times. This magmatic arc migration has been attributed to a protracted removal of material from the edge of the continent by forearc subduction erosion (Rutland, 1971).

3. Data and analysis

The seismograms used in this study were recorded by the 20 station CHILLAX seismic network (Fig. 2). Both short period and broad band stations recorded autonomously and continuously at 100 samples per second on each of three components for a period of about 14 months. We note that the CHILLAX deployment largely overlaps the 37 station OVA99 deployment of three-component short period seismometers conducted by DGF and the French GéoAzur laboratory between November 1999 and January 2000 (Marot et al., 2013). We attempted a joint analysis of the CHILLAX dataset with body wave arrival times from an OVA99 catalogue made available to us. However, the results are not significantly different from those we obtained from an independent analysis of the CHILLAX data. For that reason, and partly because we could not verify the provenance of uncertainty estimates of the arrival times the OVA99 catalogue, we report only on the analysis of the CHILLAX dataset here.

3.1. Local earthquake catalog generation

We created an aftershock catalogue for the CHILLAX deployment using a software package written expressly for this purpose by one of the authors (Roecker) called the Regressive ESTimator (REST), the details of which may be found in the supplementary material. REST locates events via grid search, and hence includes only those hypocenters that occur within a specified model volume. In the case of CHILLAX, we define that volume to be between 28°–31°S, 72°–68°W, and from the surface to 120 km depth. Processing of the entire continuous dataset resulted in about 100,000 events located within the model with about 250,000 P and 200,000 S arrival times. From this initial catalog we chose a subset based on the following criteria: (1) maximum azimuthal gap of 180° (to ensure that all events are located within the aperture of the recording stations), (2) no fewer than 12 associated phases, (3) no fewer than 2 associated S arrivals, (4) a residual threshold per phase that is the maximum of 1 s and 5% of the total travel time, and (5) a maximum standard deviation of all associated residuals of 0.80 s. Application of these criteria to the original CHILLAX catalog resulted in a refined dataset of about 9,000 events that includes 108,000 P and 101,000 S arrival times.

Despite the fact that much of the main shock rupture occurred outside of the CHILLAX network, our exclusion of any event located outside the aperture of the stations recording that event is motivated by the potential influence of (unmodeled) lateral heterogeneity on their location estimates. Tests with real and synthetic arrival times suggest that the anticipated steep gradient to higher wavespeeds west of the network, related to the transition from continental to oceanic crust and mantle, can cause hypocenters to be mislocated deeper by 10–20 km. Comparisons of teleseismic and local event depths for hypocenters east of the network suggest a similarly profound influence of unmodeled heterogeneity (Comte et al., 2016), although the nature of this heterogeneity to the east is presently unknown. As our ignorance of these wavespeed variations could lead to gross misinterpretation of trends observed in hypocenters as well as the images they produce, we excluded arrivals from hypocenters east of the CHILLAX network.

We also use REST to estimate polarities of P wave first motions and use these with the FOCMEC algorithm[2] (Snoke, 2003) to determine a range of possible double couple mechanisms. For this dataset we used unity weighting with a maximum of one polarity error allowed. We require events to have polarities reported by at least 17 stations, meaning that any mechanism shown here is consistent with at least 16 reported polarities. Emergent arrivals (defined as $1 < \mathrm{SNR} < 5$) were included only if a suitable solution could not be recovered with impulsive arrivals ($\mathrm{SNR} > 5$) alone. Mechanisms with multiple solutions without a consistent dip angle (within a range of 60°) were eliminated outright, and the remainder subjected to visual inspection. A total of 550 mechanisms were generated in this fashion (Table S1), of which 378 used only impulsive arrivals.

3.2. Arrival times from events at teleseismic distances

Relative arrival times of 480 P arrivals from 67 events that occurred at distances of 30°–90° during the time of the CHILLAX deployment were generated using a cross-correlation technique

[2] Package URL: http://www.iris.edu/pub/programs/focmec/.

similar to that described in Li et al. (2009) and VanDecar and Crosson (1990). These times are inverted jointly with the other types of observations using a technique similar to that described in Roecker et al. (2017).

3.3. Rayleigh wave dispersion curves from ambient noise

Continuous data from the ∼12 month broad band phase of the CHILLAX deployment were used to generate phase dispersion curves for fundamental mode Rayleigh waves from ambient noise. The preprocessing steps follow those described in Bensen et al. (2007) and Comte et al. (2016). Day volumes are cross-correlated, and then stacked using a phase weighted filtering approach similar to that of Baig et al. (2009), with the difference that we use a continuous rather than discrete S transform. Dispersion curves are generated using an algorithm based on that described by Ekstrom et al. (2009) using Aki's spectral formulation (Aki, 1957). Outliers are suppressed by generating phase velocity maps with the raw observations and then integrating the delay times between station pairs. These integrated times then constitute the observations we use to determine wavespeeds.

3.4. Joint inversion

The procedure used to jointly invert arrival times from locally recorded P and S body waves with relative arrival times of P waves from teleseismic events and phase delays of fundamental mode Rayleigh waves from ambient noise is virtually identical to that described in Comte et al. (2016) and Roecker et al. (2017). To briefly summarize: a 3D model is specified on a grid within a section of a spherical (geocentric) Earth. The forward problem for travel time computation uses the eikonal equation solver described in Zhang et al. (2012). Rayleigh wave phase delays are computed using the locked mode technique of Gomberg and Masters (1988). The inverse procedure consists of expanding the expressions for the observations (arrival time or phase delay) in a Taylor series and keeping the first (linear) term, using the chain rule as needed to generate expressions for sensitivity to hypocenter, Vp, and either Vs or the Vp/Vs ratio. The resulting series of equations is solved using LSQR (Paige and Saunders, 1982) with a single regularization term. Each observation is weighted in accordance with its expected uncertainty. Sensitivities for variables of different dimensions (e.g. hypocenters and wavespeeds) are scaled to have approximately the same order of magnitude in values. Models are iteratively perturbed until the reduction in the variance of residuals is insignificant. The results shown here are obtained after 12 iterations.

4. Results

4.1. Starting model

We construct a starting model combining Vs determined from surface wave dispersion and a Vp/Vs of 1.757 determined from a Wadati plot of Tp vs Ts – Tp for the entire set of body wave arrivals (Fig. S1). Sensitivities of phase delays were too small to allow reasonable variations in Vp to be resolved. To mitigate possible bias on the results due to a particular 1D starting model, we performed inversions with two models adapted from the literature. The first is based on the results of Marot et al. (2014), whose investigation was at a latitude similar to that of this study, although over a much larger range of longitude. The second is based on results from a part of northern Chile studied by Comte et al. (2016). Each of these starting models converged to similar 1D models (Fig. S2), and we used each of these 1D models as starting models for the 3D inversion. The difference between the two sets of results is minor and the difference in variance of the fit to all types of observations used (surface waves, local P and S and teleseismic P body waves) is less than 2%.

4.2. Progressive joint inversion

Because of differences in sensitivities and uncertainties, it can be advantageous to add different types of observations progressively rather that inverting them all together at the outset (e.g., Comte et al., 2016; Roecker et al., 2017). In this case, however, we found that the best results were obtained by inverting all data types together, principally due to the relative sparseness of the available intra-station paths for ambient noise tomography. Allowing the surface wave observations to adjust the 3D model as an initial step led to development of artifacts in the deeper structure that are not required by the body waves and that subsequently persist throughout the iterative process. Hence, while we do not explicitly suppress these features, they affect only a small percentage of the surface wave dataset and generally are diminished in the joint inversion to the point of insignificance.

The overall variance reduction in residuals for the entire data set is on the order of 32%, and, with the exception of the teleseismic P arrivals, is close to that percentage for each individual type of observation. Surprisingly, the teleseismic P arrivals did not have a significant impact on the final model: the fit to those times is nearly the same whether they are included in the inversion or not. Thus, the signal in the teleseismic P arrivals is adequately explained by heterogeneity in the upper 90 km depth.

4.3. Tests of resolution and robustness

We performed a suite of tests to determine the resolution capabilities of our data set, following procedures used by Comte et al. (2016). These include standard checkerboard and model recovery tests wherein synthetic data are calculated in hypothetical models, contaminated with noise, and subjected to the same analysis as that used for the real data. The results (Figs. S3–S6 and accompanying discussion in the Supplementary Material) suggest that, in general, our observations are capable of resolving wavespeeds in volumes on the order of 20 km in dimension from the surface to about 90 km depth, within a region roughly corresponding to a right triangle with the bottom of the seismic zone as the hypotenuse.

Uncertainties in hypocenters and wavespeed due to noise in the data are estimated by contaminating synthetic data sets with random noise at a level anticipated for the observations. Results of these tests suggest that hypocenters are uncertain to within 2 km in any direction and wavespeeds to about ±0.2 km/s.

We typically invert for Vp and Vp/Vs rather than Vp and Vs, on the assumption that, when dealing with null, or at least reduced, observations for either Vp or Vs in any part of the model, the ratio between the wavespeeds is more likely than either Vp or Vs themselves to be preserved. To test the implications of this assumption we compare results obtained from inverting for Vp and Vs with those from inverting for Vp and the Vp/Vs (Figs. S3–S6 in the Supplementary Material). We find that in some cases (the checkerboards) using Vs or Vp/Vs gives practically the same result, but in others (the recovery test) the use of Vp/Vs gives a more robust and accurate result (Fig. S6). Because the recovery test is a closer representation of the actual inverse problem, we focus on the model generated from Vp and Vp/Vs here.

4.4. Earthquake locations

Hypocenters are relocated at every iteration of the joint inversion. Because of the aperture constraint on location quality,

artificial "edges" appear in the hypocenter plots where these bounds, which correspond approximately to the coast and the Chile–Argentina border in the high Andes, are exceeded (Fig. 2). Hence, this data set does not include the areas of highest moment release to the west or the flat slab region beneath Argentina to the east. Nevertheless, the hypocenters retained after inversion are well positioned to investigate the nature of the subduction wedge beneath Chile in the study region.

In map view (Fig. 2) the distribution of hypocenters appears fairly uniform as a function of latitude, decreasing in density from the shallower rupture-related activity in the west to deeper ambient background activity in the east. Viewed in cross section (Figs. 3 and S7), one can distinguish four distinct zones for these locations (Fig. S8). Starting with the deeper events (zone 4 in Fig. S8), there is a plane of seismicity between 60 and 100 km depth that is separated from the remainder by a 10–15 km wide region of little to no activity. This feature was previously identified in the literature (e.g. Marot et al., 2013) as the lower plane of a double seismic zone. At depths greater than about 55 km, the upper part of the double seismic zone (zone 3 in Fig. S8) appears as a well-defined plane. Both upper and lower planes dip about 20° to the east. The seismicity above the upper plane at depths between 30 and 55 km (zone 2 in Fig. S8) represents by far the highest rate of activity that occurred after the main shock; nearly 75% of all the events recorded by CHILLAX are located in this region. Remarkably, most of this highly active zone appears to be distinct from the upper plane of the putative double seismic zone, particularly in the sections south of 31°S (Fig. S7). Where the seismicity in zone 2 displays a preferred orientation, it appears to dip about 30°–35° to the east, or some 10°–15° steeper than the double seismic zone. The fourth zone of seismicity (zone 1 in Fig. S8) is a diffuse distribution of seismicity extending up from the "high aftershock rate" region of zone 2 to the surface.

4.5. Focal mechanisms

In the context of the four zones described above, the 550 focal mechanisms determined here reveal some general patterns that provide clues as to what they represent. Mechanisms in the uppermost (zone 1) and lowermost (zone 4) zones both show predominately normal faulting (Figs. 4a and 4h). Those in zones 2 and 3 (Figs. 4b–4g) are a mixture of thrust and normal events that requires additional parsing. We note that the largest magnitude events ($M > 4$) are confined to a fairly narrow and well-defined planar region at the bottom of zone 2 and the top of zone 3 (Figs. 4f and 4g), and are nearly all thrusts with similar mechanisms. The events located in the dense cloud of activity in zone 2 above this plane (Figs. 4b–4e) tend to be smaller in magnitude and, as magnitude decreases, more likely to be associated with normal faulting. Similarly, the mechanisms for events below this plane in zone 3 (Fig. 4g) are more likely to show normal faulting, as are all the events in this zone that occur down dip of zone 2 at depths greater than about 60 km (Figs. 4g and 4h).

4.6. Wavespeed model

To first order, the wavespeed model determined by the joint inversion (Figs. 3 and S7) is simple. Viewed in cross section, the main features are two prominent gradients in both Vp and Vp/Vs associated with the lower boundaries of hypocenter zones 1 and 2. While these gradients are not sharp (because they integrate structure along path, arrival time inversions generally do not yield clear distinctions between sharp interfaces and gradual gradients), the east dipping gradient coincides with the boundary between zones 2 and 3, while the west dipping gradient bounds the eastern extent of the bulk of crustal seismicity in zone 1. These two gradients intersect at a plane associated with the larger events at about 55 km depth (dashed lines in Fig. 3) and, with the surface, bound a triangular prism. The Vp/Vs ratio within this prism (1.73) is on the low side, increasing to 1.78 outside of the prism. Vp/Vs decreases slightly from 1.78 in the upper part of the double seismic zone in zone 3, to 1.76 in zone 4. Finally, although Vp and Vs are both slightly lower than normal mantle in the region above the seismic zone at depths greater than about 60 km, that area appears to have no significant Vp/Vs anomaly.

5. Discussion

5.1. The rupture surface and upper plate faulting

The interface between a subducting oceanic lithosphere and an overriding continent is often taken to correspond to the shallowest ambient seismicity, as these events are presumed to be associated with the colder subducting plate. For example, in their study of seismic activity in this region, Marot et al. (2014) chose to draw the plate boundary above that part of the seismic zone referred to herein as zone 2, implying that the top of that zone corresponds to the rupture surface of the Illapel earthquake.

The significantly higher rate of aftershock activity in the upper part of zone 2 is consistent with a genetic relation to the main shock. However, associating these events with a main shock rupture surface is problematic. For example, the shallow depth and steep dip (35°) of this zone of aftershocks require a convoluted, non-planar interplate surface if all these aftershocks are construed to have occurred along or beneath the interplate contact (Fig. 3). The Illapel main shock centroid is not co-planar with the surface defined by the zone 2 aftershocks. A second issue is the complicated mix of thrust and normal focal mechanisms in the upper part of zone 2, along with the somewhat steep (40°–50°) dips of the eastward dipping plane of thrust events in this zone (Figs. 4b–4e and S9). A third complication is the location of much of this zone within a low wavespeed channel above – and increasingly shallow as one moves south – a steep gradient that presumably delimits the higher wavespeeds of the Nazca plate (Figs. 3 and S7).

To develop a hypothesis that is consistent with this combination of locations, mechanisms, and wavespeeds, we first note that nearly all of the larger aftershocks (those with $M > 4$) are located near the interface between zones 2 and 3 and define a narrow plane dipping about 26°E. A projection of this trend to the west is close to the mainshock centroid and the dip is close to that of the main shock mechanism (22°). This plane is also collocated with the east-dipping gradient in wavespeeds (Figs. 3 and S7), suggesting that it corresponds to a contrast in lithology. Finally, almost all of the aftershocks with mechanisms in this plane are thrusts with nearly identical nodal planes. Hence, we infer that this plane is the rupture surface, or, equivalently, the region between the Nazca and South American plates where intraseismic elastic strain was released during the Illapel megathrust earthquake. Consequently, the smaller events in the upper part of zone 2 occurred within the South American plate. Because the geotherm of a passive South American plate should not allow brittle failure except near the rupture surface, we infer that the earthquakes in zones 1 and 2 more likely occurred within (relatively cold) material derived from the subducting Nazca plate and accreted onto the South American plate at depths between ~20–55 km. The complex patterns in the focal mechanisms in zones 1 and 2 are consistent with the complex deformation one would expect in an accretionary environment.

We propose that the east dipping gradient in wavespeeds represents the pro-side of a subduction wedge (e.g., Malavieille, 1984; Brandon, 2004), with the subduction point (or S-point) located

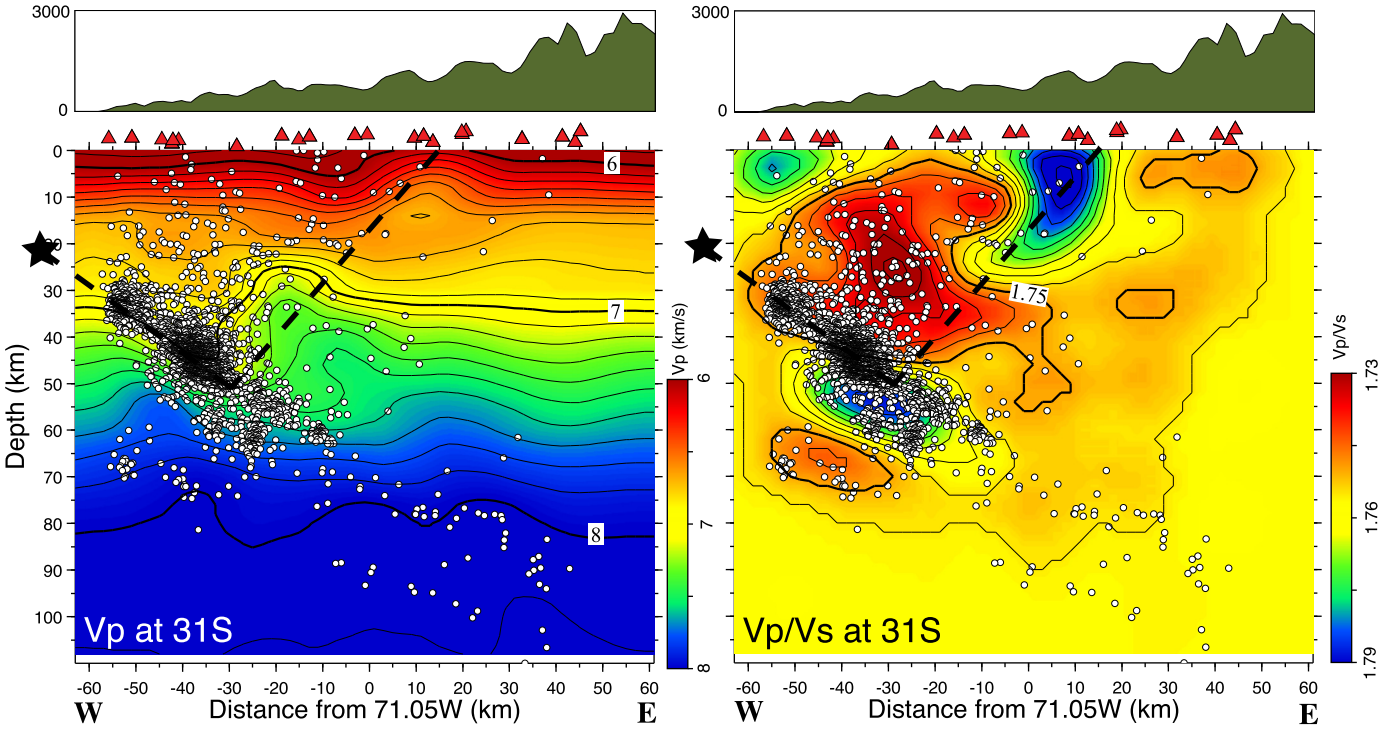

Fig. 3. EW cross sections of Vp, Vp/Vs and hypocenters at 31°S. White circles locate hypocenters within ±20 km NS of 31°S. Colors correspond to wavespeeds and ratios as indicated in the palettes to the lower right of each panel. The region of largest moment release (centroid) of the Illapel main shock shown as the black star to the left of the sections. Dashed lines outline the pro- and retro-sides of the proposed subduction wedge. Red triangles are projections of the CHILLAX network onto this section. A vertically exaggerated profile of the topography appears above each section with elevations in meters as indicated. (*Left*) Vp. The thin contour interval is 0.1 km/s, thick contours are 1 km/s and correspond, from top to bottom, to 6, 7, and 8 km/s. (*Right*) Vp/Vs ratio. The thin contour interval is 0.005, the thick contour corresponds to Vp/Vs = 1.75.

where the high rate of activity abates at about 55 km depth (Fig. 5). The S-point corresponds to the downdip limit of elastic coupling along the plate boundary, i.e., the transition between frictional and non-frictional interplate slip. In this case, the upper plate east of the wedge would act as a backstop for most of the eroded downgoing material attached to the top subducting plate (e.g., Willett et al., 1993; Beaumont et al., 1996). In fact, along the Chilean subduction margin, the retro-shear zone often presents seismicity emerging from the slab at 50–60 depth (Farias et al., 2010). The west dipping wavespeed gradient, which bounds the diffuse seismicity in zone 1 and which can be traced from the near surface to a point near the proposed S-point, would thus represent the retro-side of the subduction wedge. The preponderance of normal faulting in zone 1 is consistent with free surface extension in the top of the wedge as accreted material is underplated.

The predominant dip to the east of fault planes for thrust events in zone 2 (Fig. 4), steepens from about 30°–40° at the base of zone 2 to 40°–50° for the shallower (and smaller magnitude) events (Fig. S9), suggesting a change in deformation style from a decollement setting to distributed out-of-sequence splay faulting. The slight misalignment of the decollement fault planes with the inferred dip of the zone 2 base (26°) suggests that this part of the plate boundary may be imbricated by the splays. An uneven boundary could explain why there appears to be more activity in the upper part of zone 2 than along the rupture surface. Seismic activity within the upper part of zone 2 is evident in the ambient background (e.g., it is clearly seen in the hypocenters shown in Marot et al., 2014), but the rate significantly increased after the Illapel earthquake. This suggests that elastic strain accumulates along faults within the lower part of the wedge as part of the intraseismic cycle and is released as brittle failure. In the context of a plate margin dominated by subduction erosion, this hypothesis implies that a significant volume of the margin's leading edge – now subducted to depths of at least 30–55 km – is still largely coupled to the downgoing Nazca slab.

5.2. Corroboration with surface geology

Our proposed subduction wedge model fits well with several features observed in the surface geology, particularly those that document uplift and extension. The eastern or retro side of the subduction wedge is a west-dipping ramp that emerges about 180 km east of the trench, near the topographic break related to the front of the retro-side of the Andes (Figs. 3 and 5). The surface of the subduction wedge is characterized by a monotonically east-dipping homocline with older rocks located along the coast. The offshore region, corresponding to the pro-side, exhibits normal faulting and a small frontal accretionary complex. Normal faulting in this region is related to rapid uplift of marine terraces since about 2 Ma, suggesting strong basal accretion and thus a high static coefficient of friction on the thrust (Saillard et al., 2009).

The epicentral region of the 2015 Illapel earthquake coincides with the highest elevations along the coast and the steepest slopes of the Chilean margin offshore. The lack of a continental forearc basin in this region suggests an overlap between the Andean and Coastal wedges. The trailing edge of the Andean wedge, about 10 km east of the topographic boundary between the wedges, is also part of the homocline, suggesting that the Coastal wedge has been incorporating a part of the retro-side of the Andes since Miocene times.

The eastward tilting of the retro-side has been acquired mainly since Jurassic times, as recorded by sequential gentle angular unconformities among Mesozoic–Cenozoic deposits (Fig. 1c), long before the proposed arrival of the Juan Fernandez ridge in this area in late Miocene and before the flat slab subduction that now characterizes this part of the margin (e.g., Kay and Mpodozis, 2002). The east-dipping homocline at the retro-side is a first-order fea-

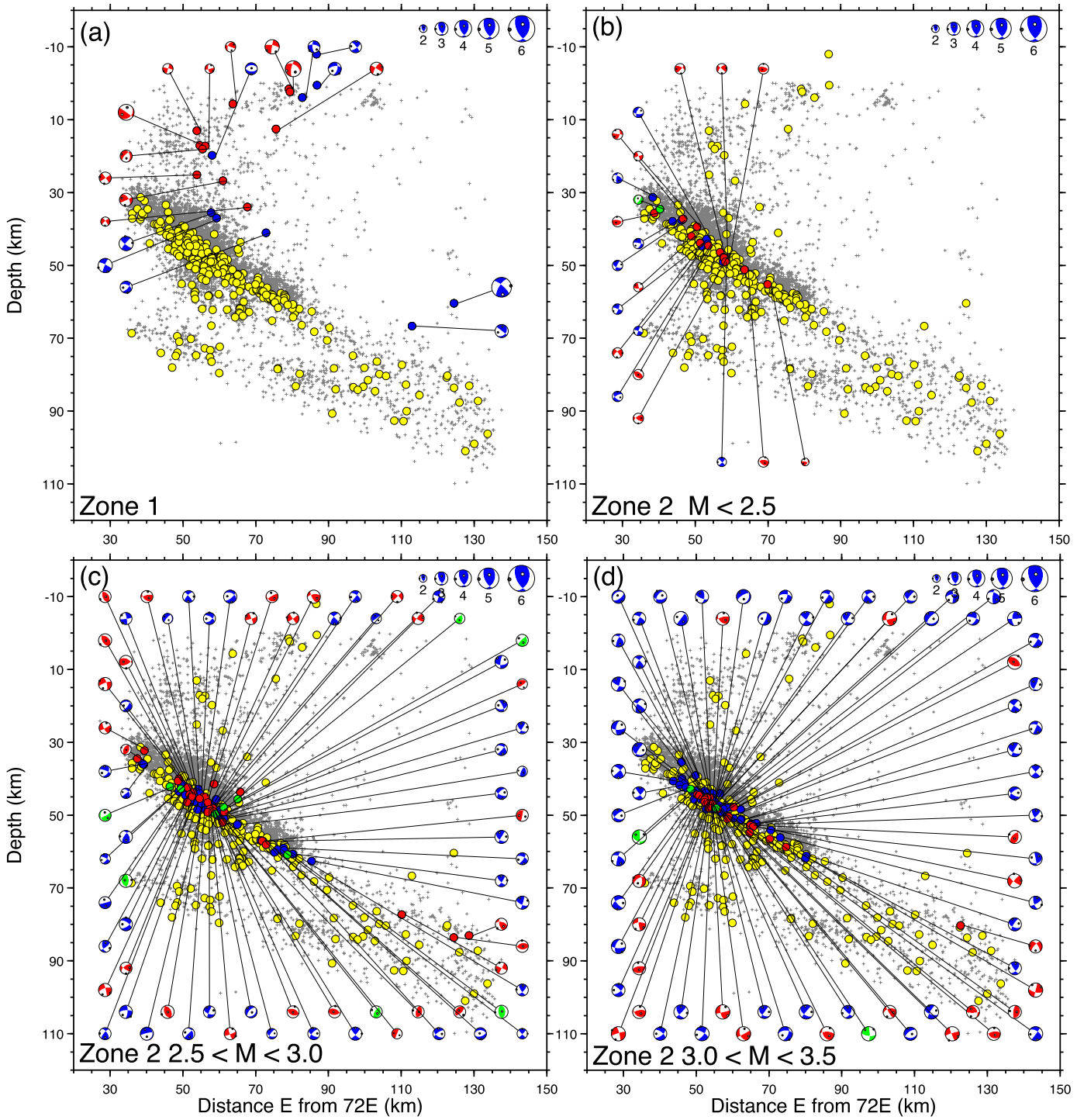

Fig. 4. EW Cross sections of focal mechanisms determined for the Illapel aftershocks. The longitudinal limits of each section are the same as those in Fig. 3. Panels show mechanisms in Zones 1–4 as indicated in the lower left corner. Because of the large number of mechanisms from Zone 2, they are binned by magnitude range as indicated. In each panel, small gray crosses locate all of the events used in the tomography, yellow circles are those events for which reasonable focal mechanisms could be determined. Mechanisms are back projected into the northern half of the focal sphere. Red, blue, and green circles and mechanisms correspond to normal, reverse, and strike-slip faulting, respectively. Earthquake magnitudes are indicated by the diameters of the mechanisms as shown in the upper right corner of each panel.

ture along the Chilean Coastal Range and is observed at many subduction complexes, such as in the western series of the Great Valley Group bounding the Franciscan complex in California (e.g., Dickinson, 2002). Therefore, we interpret the Coastal Range as a subduction complex, with both frontal and basal accretion expected to occur in the upper plate.

Neotectonic activity is documented in this area for several normal to vertical faults. The Altos de Talinay (Fig. 1b), above the patch of maximum slip, corresponds to a block bounded by antithetic normal faults cutting marine terraces that exhibit a rapid uplift since the Pleistocene (Saillard et al., 2009). The Limari river (Fig. 1) was deflected to the north due to the topographic barrier created by this uplift. As evidence of neotectonic activity, the Limari river has recaptured its original course directly to the sea, becoming a detachment-limited channel near its outlet (Fig. 1b).

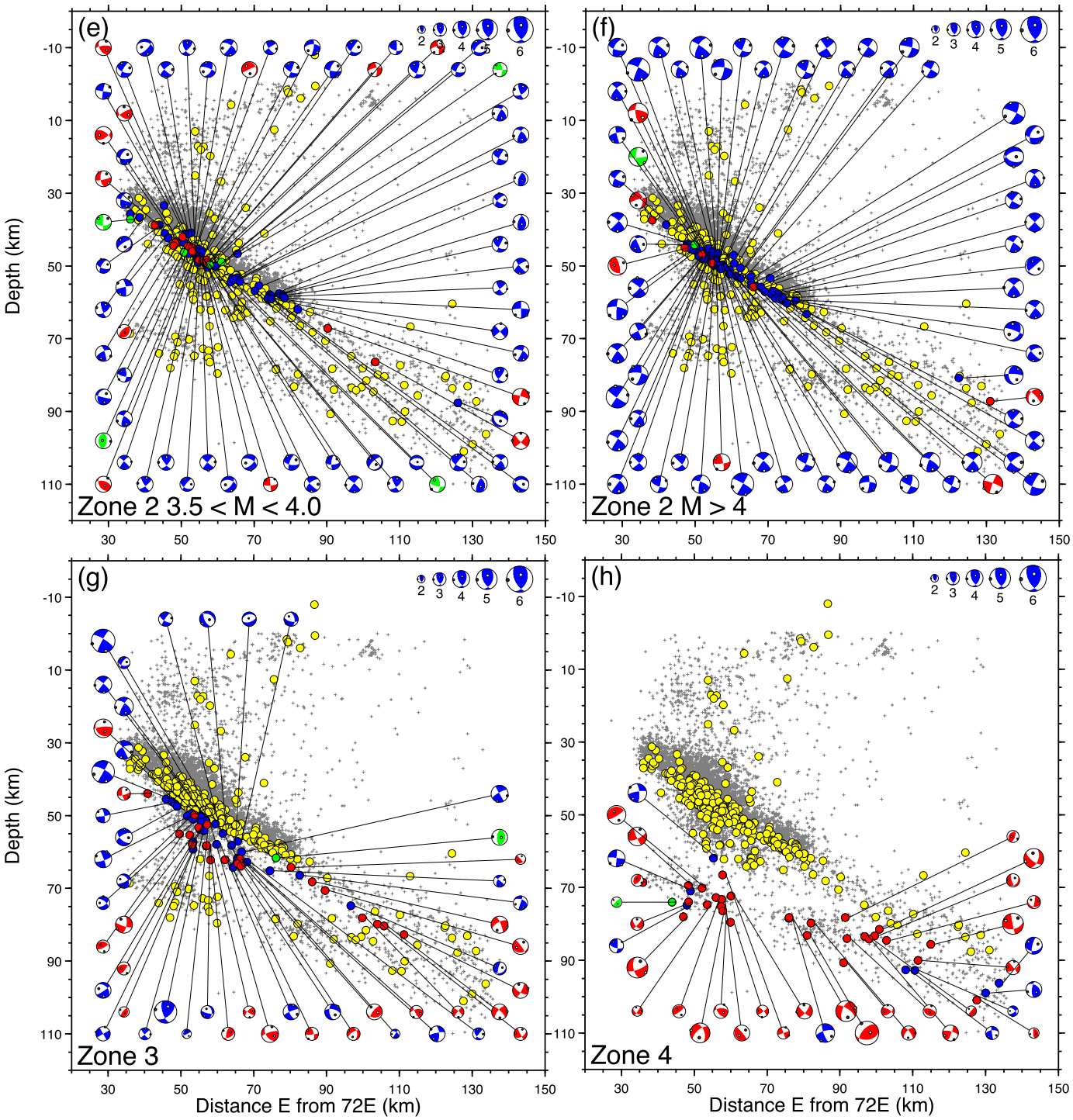

Fig. 4. (*continued*).

5.3. Implications of the wedge for subduction erosion and Andean tectonics

Our results suggest that most of the aftershocks of the Illapel rupture occurred on out-of-sequence splay faults in the upper plate. However, the type of splay faulting we envision is quite different from that typically expected in an accretionary wedge setting. In-sequence thrusting structurally decreases the topographic slope in the tapered tip of the wedge by transferring mass from the footwall to the hanging wall. In this case, extension within the wedge is shallow and a result of gravitation collapse and spreading. Instead, out-of-sequence splay thrusting in the upper part of the wedge transfers material from its footwall allowing the subducting plate to drag it downward in nappe-like fashion (Fig. 6). As it approaches the S-point, much of this material is accreted back onto the overriding accretionary complex. Additionally, rather than gravitational spreading, extensional tectonics in the uppermost part of the wedge occurs in response to underplating due to basal accretion. These shallow normal faults accommodate surface uplift in a manner often displayed along the Chile-Peru erosive margin (e.g., Saillard et al., 2009).

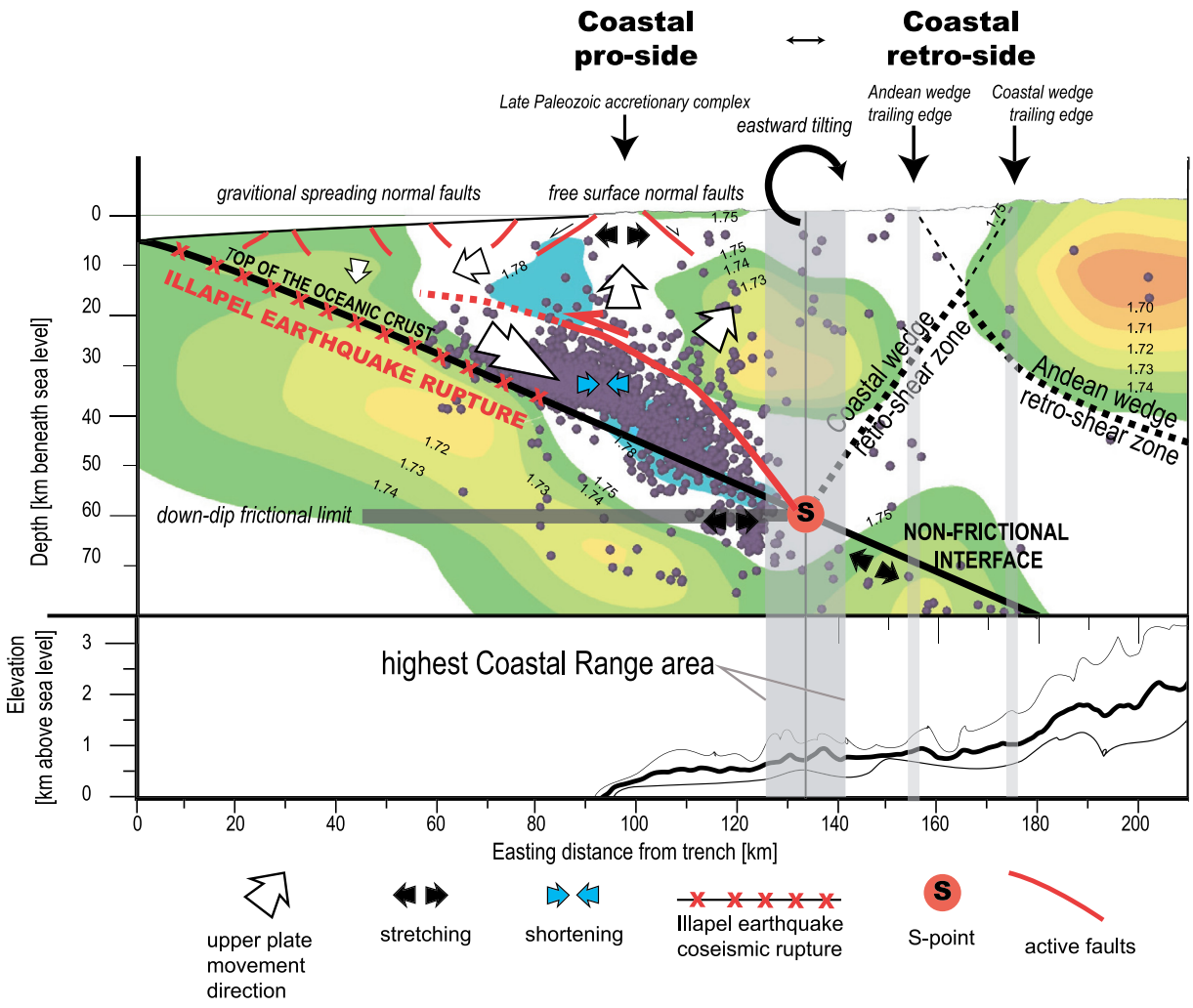

Fig. 5. Interpretation of the structural architecture of the continental margin in the Illapel region. Upper panel: As a reference background, color contours represent W-E variations in Vp/Vs at 31.5°S (Fig. S7b) and solid circles show hypocenters within ±20 km of this section. Lower panel: Minimum, mean and maximum elevations along W–E oriented profiles of topography within ±20 km of 31.5°S. The onshore Coastal wedge coincides with an east-dipping monocline that is bounded to the west by a Late Paleozoic accretionary complex (Choapa metamorphic complex shown in Fig. 1). The normal faults in this complex are related to Zone 1 seismicity and accommodate uplift as free surface extension resulting from thickening of the wedge, similar to axial stretching in a growing anticline. Deeper thickening is related to Zone 2 seismicity and occurs as a compressive stacking of crustal slices transported downward from the edge of the wedge to the S-point. Offshore normal faults are caused by gravitational adjustment after tectonic erosion of the Coastal wedge. The recycling of eroded mass at and above the S-point leads to the highest elevations of the Coastal wedge being located directly above it.

This splay faulting mechanism contrasts with the "sandpaper" or "saw-tooth" effect of seamount subduction often invoked for subduction erosion, in that, while material is removed from the upper plate in discrete "chunks", this basal erosion is not necessarily instigated by irregular structure (such as a seamount) on the subducting plate. The accretion of material back onto the upper plate perhaps takes place as a succession of downgoing crustal nappes that induce the development of an anticlinal stack at the S-point, as suggested by sandbox experiments with high basal friction (e.g., Konstantinovskaya and Malavieille, 2011).

This wedge model has several first-order implications for Andean tectonics. First, geochemical data and mass balance indicate that some fraction of the material eroded from the upper part of the wedge will be carried into the mantle with the downgoing slab rather than accreted to the overriding plate (e.g., Kay and Mpodozis, 2002; Goss et al., 2013; Kay et al., 2014). Hence, if the wedge, and by implication the position of the S-point, is to remain stationary, the upper plate necessarily will move towards the trench so that material from the forearc basin area beyond the retro limit of the wedge will replenish it, thus extinguishing the contemporaneous magmatic arc and forming a new one (Fig. 6). This type of process has been suggested by numerical modeling on a sediment starved trench (van Dinther et al., 2012), and is consistent with the sequential pinching out to the east of Mesozoic sequences disposed with mild unconformity over an east-dipping homocline along the Coastal Range (Fig. 6). The eastward migration (i.e., younging) of the magmatic arc itself since Mesozoic times is also well documented (e.g., Aguirre et al., 1974; Parada et al., 1988). Indeed, evidence that the arc has been migrating to the east despite alternating stages of compression and extension in the back-arc region since at least the Early Mesozoic suggests that subduction erosion is the governing mechanism for this migration. We note that this scenario stands in contrast to scenarios that invoke subduction coupling as the primary mechanism for Andean uplift. Considering that the Andes result mainly from back-arc shortening due to the underthrusting of the South American lithosphere (e.g., Isacks, 1988), our results additionally suggest that there is no direct connection between the development of the subduction wedge and the Andean wedge.

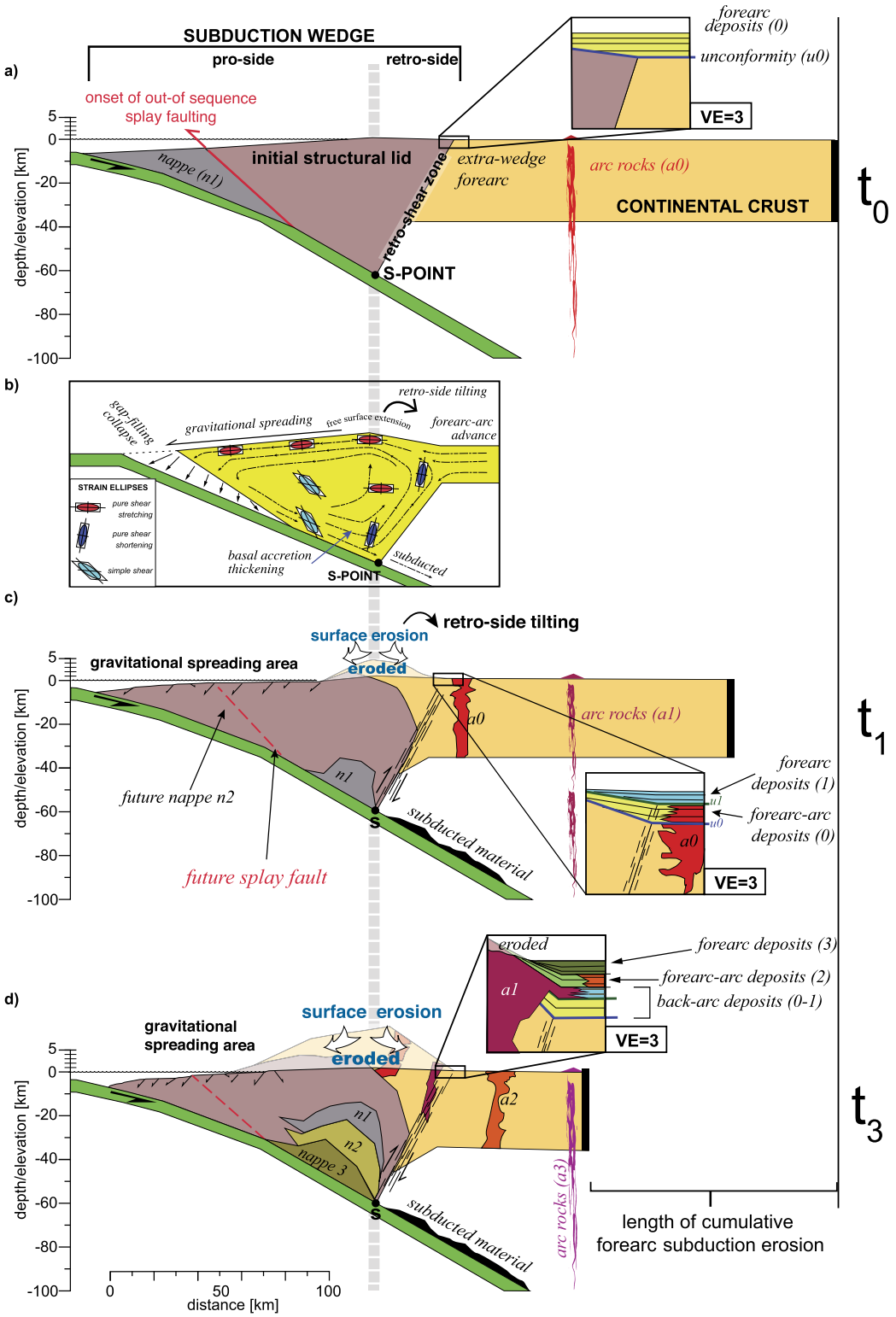

Fig. 6. General schema for tectonic erosion in a subduction margin. (a) Initially (time t_0), a subduction wedge is formed by internal shortening rather than by accretion. Basal friction will increase the taper and form an out-of-sequence splay fault on the upper plate forming a nappe (n1). The nappe is then transported downward with the subducting plate at time t_1. Forearc deposition (1) occurs over the retro-side of the wedge and beyond (zoom box). (b) Patterns of deformation produced by the downward transport of nappe n1, producing counterclockwise paths for wedge particles. Strain ellipses are shown as references for modes of deformational within the wedge (based on our results shown in Fig. 5 and on van Dinther et al., 2012). The gap left by the nappe induces the gravitational spreading of the wedge tip, incorporating part of the forearc to the structural lid at the rear of the wedge. This forearc-arc advance produces the relative migration of arc rocks and the establishment of a new magmatic arc. (c–d) Wedge evolution in stages of nappe emplacement t_1, t_2 (stage not included in detail) and t_3 including surface erosion. Gravitational spreading prevails in the wedge tip as material is extracted by subduction erosion. Nappes stacking at and above the S-point thicken the wedge, inducing uplift and free surface extension. An increase of the retro-side slope produces continuous unconformities (u1–u3) with forearc deposits (1–3) that in the rear of the wedge overlay unconformably either forearc, arc or back-arc deposits (zoom boxes). Between each stage, the upper plate, including arc rocks, migrates towards the trench as forearc subduction erosion occurs from the wedge tip. Back-arc deformation is not present, consistent with its lack of correlation with magmatic arc migration. The slope of the lower plate slope remains constant through time.

5.4. The slab below the subduction wedge

The lower part of the double seismic zone in zone 4 (Fig. 3), and the predominance of normal faulting within it (Fig. 4), was previously noted by Marot et al. (2014) and seems unambiguous. Less clear is the definition of the upper part of the double seismic zone in zone 3, at least at depths shallower than 60 km. In several of the cross sections of seismicity (Figs. 3 and S7) it appears as though the upper part of the double seismic zone lies in a region distinct from the rupture surface at the base of zone 2 seismicity. We note that this upper part of the double seismic zone lies in the middle of a region of high Vp/Vs, suggesting that these earthquakes may be related to slab dehydration.

The "mantle wedge" above the seismicity at about 50–60 km shows a decrease in Vp and Vs and a slight increase in Vp/Vs in a manner consistent with serpentinization as seen, for example, in northern Chile (Comte et al., 2016). These values are similar to those seen south of 21°N in northern Chile by Comte et al. (2016) and by analogy would correspond to about 30% serpentinization below the S-point.

Acknowledgements

This work was supported by Fondo Nacional de Desarrollo Científico y Tecnológico of Comisión Nacional de Investigación Científica y Tecnológica-Chile project 1161806, the US National Science Foundation Geophysics Program project 1600890, and by logistical and financial contributions from the Departamento de Geofísica of the Universidad de Chile, and the Advanced Mining Technology Center FB0809 PIA CONICYT. Many thanks to IRIS/PASSCAL for their help and for their quick response to our request for equipment. We were ably assisted in the field by students from the University of Florida, Rensselaer Polytechnic Institute, and the Universidad de Chile. We acknowledge the contributions of Mark Brandon, Sebastian Herrera, Daniel Carrizo, Sophie Peyrat, Gerardo Peña, Tomas Opazo, Rachel Glick, John Moore, and Emily Rodriguez. Figures were constructed using Gprofile, GMT (Generic Mapping Tools), Google Earth and Leapfrog 3D. Susan Kay and an anonymous reviewer provided very helpful and insightful reviews.

Appendix A. Supplementary material

Supplementary material related to this article can be found online at https://doi.org/10.1016/j.epsl.2019.05.033.

References

Aguirre, L., Charrier, R., Davidson, J., Mpodozis, A., Rivano, S., Thiele, R., Tidy, E., Vicente, J.-C., 1974. Andean magmatism: its paleogeographic and structural setting in the central part (30°–35°S) of the Southern Andes. Pac. Geol. 8, 1–38.

Aki, K., 1957. Space and time spectra of stationary waves with special reference to microtremors. Bull. Earthq. Res. Inst. Univ. Tokyo 35, 415–456.

Anderson, M., Alvarado, P., Zandt, G., 2007. Geometry and brittle deformation of the subducting Nazca Plate, Central Chile and Argentina. Geophys. J. Int. 171, 419–434. https://doi.org/10.1111/j.1365-246x.2007.03483.x.

Baig, A.M., Campillo, M., Brenguier, F., 2009. Denoising seismic noise cross correlations. J. Geophys. Res. 114, 1478–1512. https://doi.org/10.1029/2008JB006085.

Beaumont, C., Ellis, S., Hamilton, J., Fullsack, P., 1996. Mechanical model for subduction-collision tectonics of Alpine-type compressional orogens. Geology. https://doi.org/10.1130/0091-7613(1996)024<0675:MMFSCT>2.3.CO;2.

Becerra, J., Arriagada, C., Contreras-Reyes, E., Bascuñán, S., De Pascale, G.P., Reichert, C., Díaz-Naveas, J., Cornejo, N., 2016. Gravitational deformation and inherited structural control on slope morphology in the subduction zone of north-central Chile (∼29–33°S). Basin Res. https://doi.org/10.1111/bre.12205.

Bensen, G.D., Ritzwoller, M.H., Barmin, M.P., Levshin, A.L., Lin, F., Moschetti, M.P., Shapiro, N.M., Yang, Y., 2007. Processing seismic ambient noise data to obtain reliable broad-band surface wave dispersion measurements. Geophys. J. Int. 169, 1239–1260. https://doi.org/10.1111/j.1365-246X.2007.03374.x.

Brandon, M.T., 2004. The Cascadia subduction wedge: the role of accretion, uplift, and erosion. In: van der Pluijm, B.A., Marshak, S. (Eds.), Earth Structure, An Introduction to Structural Geology and Tectonics, second ed. W.W. Norton & Company, Inc., New York, pp. 566–574.

Carretier, S., Regard, V., Vassallo, R., Aguilar, G., Martinod, J., Riquelme, R., Pepin, E., Charrier, R., Hérail, G., Farias, M., Guyot, J.L., Vargas, G., Lagane, C., 2013. Slope and climate variability control of erosion in the Andes of central Chile. Geology 41, 195–198. https://doi.org/10.1130/G33735.1.

Charrier, R., Ramos, V.A., Tapia, F., Sagripanti, L., 2015. Tectono-stratigraphic evolution of the Andean Orogen between 31 and 37 S (Chile and Western Argentina). Geol. Soc. (Lond.) Spec. Publ. 399, 13–61. https://doi.org/10.1144/SP399.20.

Comte, D., Carrizo, D., Roecker, S., Ortega-Culaciati, F., Peyrat, S., 2016. Three-dimensional elastic wave speeds in the northern Chile subduction zone: variations in hydration in the supraslab mantle. Geophys. J. Int. 207, 1080–1105. https://doi.org/10.1093/gji/ggw318.

Dickinson, W.R., 2002. Reappraisal of hypothetical Franciscan thrust wedging at Coalinga: implications for tectonic relations along the Great Valley flank of the California Coast Ranges. Tectonics 21, 3-1–3-14. https://doi.org/10.1029/2001TC001315.

Ekström, G., Abers, G.A., Webb, S.C., 2009. Determination of surface-wave phase velocities across USArray from noise and Aki's spectral formulation. Geophys. Res. Lett. 36, 415. https://doi.org/10.1029/2009GL039131.

Farias, M., Charrier, R., Carretier, S., Martinod, J., Fock, A., Campbell, D., Cáceres, J., Comte, D., 2008. Late Miocene high and rapid surface uplift and its erosional response in the Andes of central Chile (33°–35°S). Tectonics 27, TC1005. https://doi.org/10.1029/2006TC002046.

Farias, M., Comte, D., Charrier, R., Martinod, J., David, C., Tassara, A., Tapia, F., Fock, A., 2010. Crustal-scale structural architecture in central Chile based on seismicity and surface geology: implications for Andean mountain building. Tectonics 29, TC3006. https://doi.org/10.1029/2009TC002480.

Gomberg, J.S., Masters, T.G., 1988. Waveform modelling using locked mode synthetic and differential seismograms: application to determination of the structure of Mexico. Geophys. J. Int. 94, 193–218.

Goss, A.R., Kay, S.M., Mpodozis, C., 2013. Andean adakite-like high-Mg andesites on the northern margin of the Chilean–Pampean flat-slab (27–28·5°S) associated with frontal arc migration and fore-arc subduction erosion. J. Petrol. 54, 2193–2234. https://doi.org/10.1093/petrology/egt044.

Isacks, B.L., 1988. Uplift of the Central Andean Plateau and bending of the Bolivian Orocline. J. Geophys. Res. 93, 3211. https://doi.org/10.1029/JB093iB04p03211.

Jordan, T.E., Isacks, B.L., Allmendinger, R.W., Brewer, J.A., Ramos, V.A., Ando, C.J., 1983. Andean tectonics related to geometry of subducted Nazca plate. Geol. Soc. Am. Bull. 94, 341–361. https://doi.org/10.1130/0016-7606(1983)94<341:ATRTGO>2.0.CO;2.

Kay, S.M., Mpodozis, C., 2002. Magmatism as a probe to the Neogene shallowing of the Nazca plate beneath the modern Chilean flat-slab. J. South Am. Earth Sci. 15, 39–57. https://doi.org/10.1016/s0895-9811(02)00005-6.

Kay, S.M., Mpodozis, C., Gardeweg, M., 2014. Magma sources and tectonic setting of Central Andean andesites (25.5–28°S) related to crustal thickening, forearc subduction erosion and delamination. Geol. Soc. (Lond.) Spec. Publ. 385, 303–334. https://doi.org/10.1144/SP385.11.

Konstantinovskaya, E., Malavieille, J., 2011. Thrust wedges with decollement levels and syntectonic erosion: a view from analog models. Tectonophysics 502, 336–350.

Kreemer, C., Blewitt, G., Klein, E.C., 2014. A geodetic plate motion and Global Strain Rate Model. Geochem. Geophys. Geosyst. 15, 3849–3889. https://doi.org/10.1002/2014GC005407.

Li, Z., Roecker, S., Wei, B., Wang, H., Schelochkov, G., Bragin, V., 2009. Tomographic image of the crust and upper mantle beneath the western Tien Shan from the MANAS broadband deployment: possible evidence for lithospheric delamination. Tectonophysics 477 (1–2), 49–57.

Malavieille, J., 1984. Modelisation experimentale des chevauchements imbriques; application aux chaines de montagnes. Bull. Soc. Géol. Fr. S7-XXVI, 129–138. https://doi.org/10.2113/gssgfbull.S7-XXVI.1.129.

Marot, M., Monfret, T., Pardo, M., Ranalli, G., Nolet, G., 2013. A double seismic zone in the subducting Juan Fernandez Ridge of the Nazca Plate (32°S), central Chile. J. Geophys. Res., Solid Earth 118, 3462–3475. https://doi.org/10.1002/jgrb.50240.

Marot, M., Monfret, T., Gerbault, M., Nolet, G., Ranalli, G., Pardo, M., 2014. Flat versus normal subduction zones: a comparison based on 3-D regional traveltime tomography and petrological modelling of central Chile and western Argentina (29°–35°S). Geophys. J. Int. 199, 1633–1654. https://doi.org/10.1093/gji/ggu355.

Mpodozis, C., Ramos, V., 1990. The Andes of Chile and Argentina. In: Ericksen, G.E., Cañas Pinochet, M.T., Reinemud, J.A. (Eds.), Geology of the Andes and Its Relation to Hydrocarbon and Mineral Resources. Houston. In: Circum-Pacific Council for Energy and Mineral Resources, vol. 11, pp. 59–90.

Mulcahy, P., Chen, C., Kay, S.M., Brown, L.D., Isacks, B.L., Sandvol, E., Heit, B., Yuan, X., Coira, B.L., 2014. Central Andean mantle and crustal seismicity beneath the Southern Puna plateau and the northern margin of the Chilean-Pampean flat slab. Tectonics 33, 1636–1658. https://doi.org/10.1002/2013TC003393.

Paige, C.C., Saunders, M.A., 1982. LSQR: an algorithm for sparse linear equations and sparse least squares. ACM Trans. Math. Softw. 8 (1), 43–71.

Parada, M.A., Rivano, S., Sepulveda, P., Herve, M., Hervé, F., Puig, A., Munizaga, F., Brook, M., Pankhurst, R., Snelling, N., 1988. Mesozoic and cenozoic plutonic de-

velopment in the Andes of central Chile (30°30′–32°30′S). J. South Am. Earth Sci. 1, 249–260. https://doi.org/10.1016/0895-9811(88)90003-X.

Rebolledo, S., Charrier, R.C.A., 1994. Evolución del basamento paleozoico en el área de Punta Claditas, Región de Coquimbo, Chile (31–32S). Rev. Geol. Chile 21 (1), 55–69. https://doi.org/10.5027/andgeoV21n1-a03.

Rodríguez, M.P., Charrier, R., Brichau, S., Carretier, S., Farias, M., de Parseval, P., Ketcham, R.A., 2018. Latitudinal and longitudinal patterns of exhumation in the Andes of north-central Chile. Tectonics 37, 2863–2886. https://doi.org/10.1029/2018TC004997.

Roecker, S., Ebinger, C., Tiberi, C., Mulibo, G., Ferdinand-Wambura, R., Mtelela, K., Kianji, G., Muzuka, A., Gautier, S., Albaric, J., Peyrat, S., 2017. Subsurface images of the Eastern Rift, Africa, from the joint inversion of body waves, surface waves and gravity: investigating the role of fluids in early-stage continental rifting. Geophys. J. Int. 210 (2), 931–950. https://doi.org/10.1093/gji/ggx220.

Rutland, R.W.R., 1971. Andean orogeny and ocean floor spreading. Nature 233 (5317), 252–255. https://doi.org/10.1038/233252a0.

Saillard, M., Hall, S.R., Audin, L., Farber, D.L., Hérail, G., Martinod, J., Regard, V., Finkel, R.C., Bondoux, F., 2009. Non-steady long-term uplift rates and Pleistocene marine terrace development along the Andean margin of Chile (31°S) inferred from ^{10}Be dating. Earth Planet. Sci. Lett. 277, 50–63. https://doi.org/10.1016/j.epsl.2008.09.039.

Snoke, J.A., 2003. FOCMEC: Focal Mechanism determinations. In: Lee, W.H.K., Kanamori, H., Jennings, P.C., Kisslinger, C. (Eds.), International Handbook of Earthquake and Engineering Seismology. Academic Press, San Diego (Part B: pp. 1629–1630 and accompanying CD).

Tilmann, F., Zhang, Y., Moreno, M., Saul, J., Eckelmann, F., Palo, M., Deng, Z., Babeyko, A., Chen, K., Baez, J.C., Schurr, B., Wang, R., Dahm, T., 2016. The 2015 Illapel earthquake, central Chile: a type case for a characteristic earthquake? Geophys. Res. Lett. 43, 574–583. https://doi.org/10.1002/2015GL066963.

VanDecar, J.C., Crosson, R.S., 1990. Determination of teleseismic relative phase arrival times using multi-channel cross-correlation and least squares. Bull. Seismol. Soc. Am. 80, 150–169.

van Dinther, Y., Morra, G., Funiciello, F., Rossetti, F., Faccenna, C., 2012. Exhumation and subduction erosion in orogenic wedges: insights from numerical models. Geochem. Geophys. Geosyst. 13, Q06003. https://doi.org/10.1029/2011GC004011.

von Huene, R., Scholl, D.W., 1991. Observations at convergent margins concerning sediment subduction, subduction erosion, and the growth of continental crust. Rev. Geophys. 29, 279–316. https://doi.org/10.1029/91RG00969.

von Huene, R., Corvalán, J., Flueh, E.R., Hinz, K., Korstgard, J., 1997. Tectonic control of the subducting Juan Fernández Ridge on the Andean margin near Valparaiso, Chile. Tectonics 16, 474–488. https://doi.org/10.1029/96tc03703.

von Huene, R., Ranero, C.R., Vannucchi, P., 2004. Generic model of subduction erosion. Geology 32, 913–914. https://doi.org/10.1130/G20563.1.

Willett, S., Beaumont, C., Fullsack, P., 1993. Mechanical model for the tectonics of doubly vergent compressional orogens. Geology 21, 371–374. https://doi.org/10.1130/0091-7613(1993)021<0371:mmftto>2.3.co;2.

Willner, A.P., Gerdes, A., Massonne, H.J., 2008. History of crustal growth and recycling at the Pacific convergent margin of South America at latitudes 29°–36° S revealed by a U–Pb and Lu–Hf isotope study of detrital zircon from late Paleozoic accretionary systems. Chem. Geol. 253, 114–129. https://doi.org/10.1016/j.chemgeo.2008.04.016.

Zhang, H., Roecker, S., Thurber, C.H., Wang, W., 2012. Seismic Imaging of microblocks and weak zones in the crust beneath the southeastern margin of the Tibetan Plateau. In: Dar, I.A. (Ed.), Earth Sciences. IntechOpen, London, pp. 159–202.